

# Measuring Local RF Heating in MRI: Simulating Perfusion in a Perfusionless Phantom

Imran B. Akca, BS,<sup>1</sup> Onur Ferhanoglu, MS,<sup>1</sup> Christopher J. Yeung, PhD,<sup>2</sup> Sevin Guney, MSc,<sup>3</sup> T. Onur Tasci, MS,<sup>1</sup> and Ergin Atalar, PhD<sup>1,4\*</sup>

**Purpose:** To overcome conflicting methods of local RF heating measurements by proposing a simple technique for predicting in vivo temperature rise by using a gel phantom experiment.

**Materials and Methods:** In vivo temperature measurements are difficult to conduct reproducibly; fluid phantoms introduce convection, and gel phantom lacks perfusion. In the proposed method the local temperature rise is measured in a gel phantom at a timepoint that the phantom temperature would be equal to the perfused body steady-state temperature value. The idea comes from the fact that the steady-state temperature rise in a perfused body is smaller than the steady-state temperature increase in a perfusionless phantom. Therefore, when measuring the temperature on a phantom there will be the timepoint that corresponds to the perfusion time constant of the body part.

**Results:** The proposed method was tested with several phantom and in vivo experiments. Instead, an overall average of 30.8% error can be given as the amount of underestimation with the proposed method. This error is within the variability of in vivo experiments (45%).

**Conclusion:** With the aid of this reliable temperature rise prediction the amount of power delivered by the scanner can be controlled, enabling safe MRI examinations of patients with implants.

**Key Words:** RF heating; MRI safety; interventional MRI; metallic implants; perfusion; bioheat equation  
**J. Magn. Reson. Imaging 2007;26:1228–1235.**  
 © 2007 Wiley-Liss, Inc.

THE RISK OF HAZARDOUS RF heating when doing MRI scans with metallic objects present in the body is well reported. The potential for RF heating is particularly great for long linear conductive objects, such as guidewires and minimally invasive imaging antennas (1–3).

Most published studies of RF heating with such devices have measured temperature changes in fluid or gel phantoms (4–10). However, the temperature increases measured in such phantom studies do not accurately reflect the temperature increases that can occur in living patients, primarily because the physiologic effects of bioheat transfer have not been taken into account (11).

The sources of error are several. First, as Smith et al (12) demonstrated, the choice of phantom material has a significant effect on the measured temperature changes in such phantom experiments. Studies that have used fluid phantoms (water or saline) (4–7) introduced the possibility of convective heat transfer (a non-physiologic phenomenon in most tissues), which nonlinearly limits the potential temperature increase, resulting in significant underestimation of the temperature change. Studies with gel phantoms (8–10) removed the possibility of convection but can still significantly overestimate (100% or more) or underestimate (50% or more) the temperature change if the gel's thermal conductivity differs from that of the body (12).

Second, no phantom study has attempted to model a crucial heat transfer component—perfusion. All living tissues in the body are perfused, although some, like the eye and cortical bone, have very low perfusion. A worst-case heating scenario has very low perfusion, not zero perfusion (13). Perfusion is a significant component of bioheat transfer that, if ignored, will result in overestimation of the temperature change. This overestimation is exacerbated for larger phantoms.

One approach to overcome these limitations has been to measure specific absorption rate (SAR) in phantom studies (14,15) rather than temperature change. Measurements of SAR, which is proportional to the *initial rate* of temperature increase, are much less susceptible

<sup>1</sup>Electrical and Electronic Engineering Department, Bilkent University, Ankara, Turkey.

<sup>2</sup>Division of Intramural Research, National Heart, Lung & Blood Institute, National Institutes of Health, Bethesda, Maryland.

<sup>3</sup>Institute of Health Sciences, Department of Physiology, Gazi University, Ankara, Turkey.

<sup>4</sup>Department of Radiology, Johns Hopkins University School of Medicine, Baltimore, Maryland.

I.B. Akca is now with Institute of Material Science and Nanotechnology, Physics Department, Bilkent University, Ankara, Turkey.

O. Ferhanoglu is now with the Department of Electrical and Electronics Engineering, Koc University, Istanbul, Turkey.

T.O. Tasci is now with the Department of Bioengineering, University of Utah, Salt Lake City, Utah.

Contract grant sponsor: National Institutes of Health; Contract grant number: R01 RR 15396; Contract grant sponsor: European Commission; Contract grant number: FP6 Marie Curie International Reintegration Grant.

\*Address reprint requests to: Ergin Atalar, PhD, Bilkent University, Department of Electrical and Electronics Engineering, Bilkent 06800, Ankara, Turkey. E-mail: ergin@ee.bilkent.edu.tr

Received March 17, 2007; Accepted August 3, 2007.

DOI 10.1002/jmri.21161

Published online in Wiley InterScience (www.interscience.wiley.com).

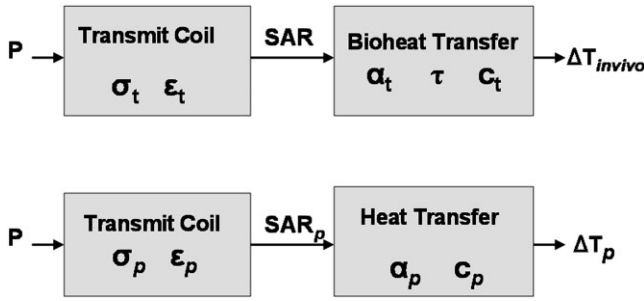


**Figure 1.** Top row: Generalized schematic of RF heating of patients in an MRI scanner. Power,  $P$ , from the RF transmitter is deposited in the tissue as a specific absorption rate distribution (SAR). This is in turn transformed into a local temperature increase,  $\Delta T$ , depending on the electrical conductivity,  $\sigma$ , and the electrical permittivity,  $\epsilon$ , the thermal diffusivity,  $\alpha$ , perfusion time constant,  $\tau$ , and heat capacity,  $c$ . Bottom row: Schematic diagram of RF heating of gel phantoms in an MRI scanner. Electrical conductivity, electrical permittivity, thermal diffusivity, and heat capacity may not exactly match physiologic values. Perfusion is typically absent.

to the heat transfer conditions. Therefore, phantom measurements are more likely to properly simulate physiological conditions. However, it is temperature, and not SAR, that ultimately causes tissue damage. Thus, the conclusions of these studies are also limited.

The goal of this study is to demonstrate a method for accurately predicting in vivo temperature changes near metallic implants during MRI, rather than simply measuring the raw temperature changes that can be generated in a nonphysiologic phantom material. This method is able to simulate the effects of physiologic thermal conductivity and perfusion in a phantom that has no actual perfusion (nor necessarily even the correct thermal conductivity), thus providing an unambiguous measure of a metallic device’s RF safety.

**MATERIALS AND METHODS**

Figure 1 summarizes the limitations of phantom studies. Top row of Figure 1 shows the transfer of RF power,  $P$ , from the RF transmitter (usually body coil), into an SAR distribution in the patient and ultimately to a temperature increase,  $\Delta T$ , during a normal clinical MRI scan on a living patient. The SAR distribution depends primarily on the geometric positioning of the patient relative to the transmitter and the tissue’s electrical properties: electrical conductivity,  $\sigma$  and electrical permittivity,  $\epsilon$ . The SAR distribution is converted to a temperature distribution, depending primarily on the tissue’s thermal properties: thermal diffusivity,  $\alpha$ , and perfusion time constant,  $\tau$  (time constant of temperature rise when the tissue is exposed to uniform heating). Bottom row of Figure 1 shows how a phantom experiment typically fails to account for all the factors that affect the measured temperature increase. Usually the electrical properties of the tissues are adequately modeled by a tissue-equivalent lossy dielectric. However, the thermal properties of the phantom are neglected: the thermal conductivity is typically unknown, and there is no perfusion.

**Predicting Perfused Body Temperature Rise Using Perfusionless Phantom Temperature Data**

The new method proposed here is summarized in Fig. 2. In this method the local temperature rise is measured in a gel phantom at a timepoint that the phantom temperature would be equal to the perfused body steady-state temperature value. The idea comes from the fact that the steady-state temperature rise in a perfused body is smaller than the steady-state temperature increase in a perfusionless phantom. The timepoint that the phantom temperature equals to the perfused body steady-state temperature value may depend on the heat distribution. Here we will first calculate this timepoint for a uniform heating case and then investigate the errors resulting from using the same timepoint for predicting the perfused body steady-state temperature rise.

The bioheat transfer equation (16) describes how an SAR distribution is converted to a distribution of temperature change,  $\Delta T$ , in the presence of conduction and perfusion heat transfer:

$$\frac{d\Delta T(\vec{r}, t)}{dt} = \alpha \nabla^2 \Delta T(\vec{r}, t) - \frac{1}{\tau} \Delta T(\vec{r}, t) + \frac{1}{c} \text{SAR}(\vec{r}) \quad (1)$$

where  $r$  and  $t$  are the space and time coordinates, respectively,  $\alpha$  is the thermal diffusivity,  $\nabla^2$  is the Laplacian operator,  $c$  is the heat capacity,  $\tau$  is the perfusion time constant ( $\tau = c/c_b/\rho_b m$ , where  $\rho_b$  is the mass density of the perfusing blood,  $c_b$  is the heat capacity of the blood, and  $m$  is the volumetric flow rate of blood per unit mass of tissue). This equation models the physiologic system labeled “Bioheat Transfer” in Fig. 1, top row.

When the heating is uniform, the Laplacian term of Eq. (1) is zero. The steady-state temperature becomes

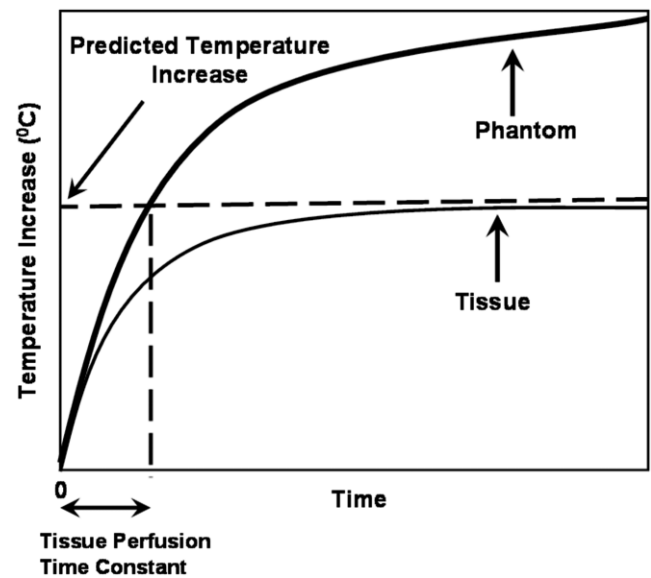


**Figure 2.** Pictorial representation of the proposed theorem: On the phantom graph, the temperature increase at tissue perfusion time constant is equal to temperature increase of in vivo case at the steady state.

$\tau/cSAR$ . On the other hand, uniform heating of a perfusionless phantom has no steady-state value and the temperature rise is  $t/cSAR$ . Therefore, the temperature of the perfusionless phantom becomes equal to the steady-state temperature of the perfused body when time is equal to the perfusion time constant,  $\tau$ .

When the heating is not uniform, the analysis is rather involved. It was previously shown that for the special case of localized RF heating in deep tissues, the type that occurs with invasive or implanted metal objects, this equation can be reduced to a linear, shift-invariant system. As such, it is fully characterized by its impulse response function, also called Green's function (2). The bioheat equation can be solved, then, by simply convolving the SAR distribution by this Green's function to yield the resulting temperature distribution, shown here for steady-state conditions (2):

$$\Delta T_{ss}(\vec{r}_0) = \int SAR(\vec{r})G(\vec{r} - \vec{r}_0)dV \quad (2)$$

where the integral is performed over the whole volume,  $V$ , and  $G$  is the Green's function given in spherical coordinates as (2):

$$G(r) = \frac{1}{4\pi\alpha_t c_t r} e^{-\nu r} \quad (3)$$

where  $\nu = 1/\sqrt{\alpha_t \tau}$  is a lumped perfusion constant. In this equation tissue-specific parameters are denoted by subscript  $t$ . The Green's function represents the temperature distribution in the body resulting from a point SAR source. The temperature increase at any position,  $\vec{r}_0$ , is a weighted average of the local SAR distribution. For example, in the case of a spherically symmetric SAR distribution centered at the origin, this integral becomes:

$$\Delta T_{ss}(0) = \int_0^\infty SAR(r)G(r)4\pi r^2 dr \quad (4)$$

where  $r$  is the radius,  $4\pi r^2$  is the Jacobian.

Spatial 3D Fourier transform of the Green's function yields the following:

$$G(\xi) = \frac{\tau}{c_t} \frac{1}{1 + \frac{\xi^2}{\nu^2}} \quad (5)$$

where,  $\xi$  is the spatial radial frequency variable of the Fourier transform. We will compare this value with the phantom measurement value.

In a perfusionless phantom with identical thermal conductivity and diffusion as in the in vivo case, the Green's function takes the following time-dependent form (2):

$$G(r, t) = \frac{1}{c_p(4\pi\alpha_p t)^{3/2}} \exp\left(-\frac{r^2}{4\alpha_p t}\right) \quad (6)$$

which represents temperature distribution in a phantom as a function of time when an impulse SAR is applied to a point at the center of the phantom. In this equation, phantom-related parameters are denoted by subscript  $p$ .

When a unit step heating is applied to a point at the center of a phantom for a period of time,  $\tau$ , which is the perfusion time constant of the tissue of interest, the phantom temperature distribution can be found as:

$$G_p(r) = \int_0^\tau G(r, t) dt \quad (7)$$

In order to compare this perfusionless phantom temperature distribution with in vivo temperature distribution, we take its 3D spatial Fourier transform:

$$G_p(\xi) = \frac{\tau}{c_p} \frac{1 - \exp(-\xi^2/\nu_p^2)}{\xi^2/\nu_p^2} \quad (8)$$

where

$$\nu_p = 1/\sqrt{\alpha_p \tau}$$

As can be seen, Eqs. (5) and (8) are different. A careful analysis of these equations, however, yields striking similarities. If one assumes that the thermal diffusion constants and the heat capacity of the gel phantom are designed to be equal to that of tissue ( $c_t = c_p$ ,  $\alpha = \alpha_p$ ), the coefficients of these equations become equal. In addition, this assumption makes lumped perfusion constants equal ( $\nu = \nu_p$ ). Both functions given in Eqs. (5) and (8) depend only on the radial component of the frequency normalized with the lumped perfusion constant,  $\nu$ . The functions  $(1 - \exp(-\xi^2))/\xi^2$  and  $1/(1 + \xi^2)$  are very similar functions (Fig. 3a), showing a maximum deviation of 30% when the radial spatial frequency is  $1.34\nu$  (Fig. 3b). This means that when a gel phantom temperature measurement is conducted at the time of perfusion time constant, the maximum possible overestimation is 30%.

For both Green's functions (phantom and in vivo cases),  $c_t$  and  $c_p$  are simple scaling functions. In cases where the heat capacity of the phantom and tissue do not match, the mismatch can be corrected by simple scaling of the phantom temperature using  $c_p/c_t$  ratio. Typical values of this ratio are in the range of 1 to 3 (Table 1).

Here is the proposed algorithm:

1. Make a gel phantom that matches as closely as possible the geometric, electrical properties and the thermal conductivity of the situation in which the metallic device will be used. The electromagnetic part of the problem, particularly geometry, electrical permittivity, and electrical conductivity, must be properly simulated physically. Fortunately, this is what many studies have already attempted to do. One may want to orient the device relative to the RF transmitter in a way that will generate the worst-case *coupling*, not necessarily

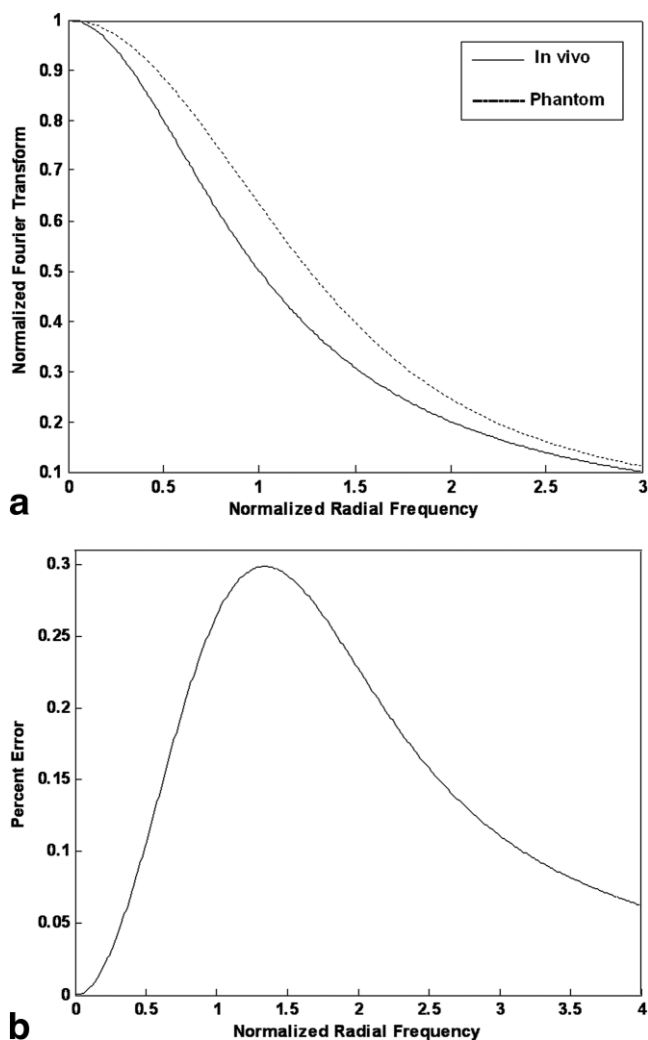


**Figure 3. a:** Comparison of Fourier transform of in vivo Green's function with phantom Green's function. Both X and Y axes are normalized for ease of comparison. **b:** Percent error in the phantom measurement as a function of normalized frequency. Maximum deviation when the radial spatial frequency is  $1.34\nu$  should be noted.

worst-case absolute *heating* (adjustments such as moving the phantom off-center or changing the depth of the device in the phantom can be accounted for in Step 5).

2. Appropriately position the selected temperature probe at the suspected hotspots and record the temperature rise at the hotspots as a function of applied SAR.

3. Report the temperature rise after the power has been applied for  $\tau$  seconds, where  $\tau$  is the perfusion time constant of the tissue in which the metallic device will be placed. This temperature is the expected in vivo temperature rise. Values for perfusion time constants can be from Table 1 or derived from literature tables (17–22).
4. Optional: Correct the estimated temperature increase with the ratio of the heat capacity of the phantom and tissue. Values of heat capacity can be obtained from the literature or from Table 1. This scaling step is not necessary if the estimated temperature is normalized with measured SAR at one other point on the phantom (as in Step 5.) Otherwise, scaling is necessary.
5. If measuring the safety of a passive device that is completely inside the body, measure the applied SAR in the region of hotspots with the exact same configuration except with the metallic device removed, and normalize the predicted in vivo temperature rise with the applied SAR yielding the safety index (23). Without this normalization step the value reported in Step 3 will only be applicable to the specific geometry configured in Step 2. Certain geometric effects such as moving the phantom off-center or changing the depth of the object in the phantom will change the absolute amount of heating measured near the device, but this will be caused by a proportional change in the heating at the same location without the device in place. These effects can be accounted for with this normalization step. The normalized temperature rise, namely the safety index (23), has previously been shown to be a measure of the possible in vivo temperature change that can occur with a metallic device, which is independent of geometry.

We have tested the algorithm with in vivo experiments. With a copper wire of length 110 cm as the ablation probe, we compared predictions of in vivo temperature change in agarose gel phantom experiments with the actual temperature rise measured in various tissues in live rabbits.

**Experimental Design Considerations**

The experimental set-up is shown in Fig. 4. A 110-cm, 1-mm diameter copper wire was inserted 1.5 cm into the tissue/phantom to induce current that causes temperature increase near the tip of the wire. The position and orientation of both the wire and the rabbit within the scanner bore affect the coupling of the wire to the

Table 1  
Thermal Properties of Different Tissues of Rabbit

Tissue Type (rabbit)	Perfusion (mL/100g/min)	Time Constant (sec)	Tissue Heat Capacity ( $c_v$ ) (J/kgK)	Thermal Diffusivity ( $\alpha$ ) ( $\text{cm}^{-2}/\text{sec}$ )	References
Fat	9–13	275–396	2500	0.1	27, 32
Brain	35–75	72–150	3700	0.143	27, 31
Liver	65–234	22–85	3600	0.136	27, 28, 29
Kidney	200–500	12–30	3900	0.128	27, 29, 30



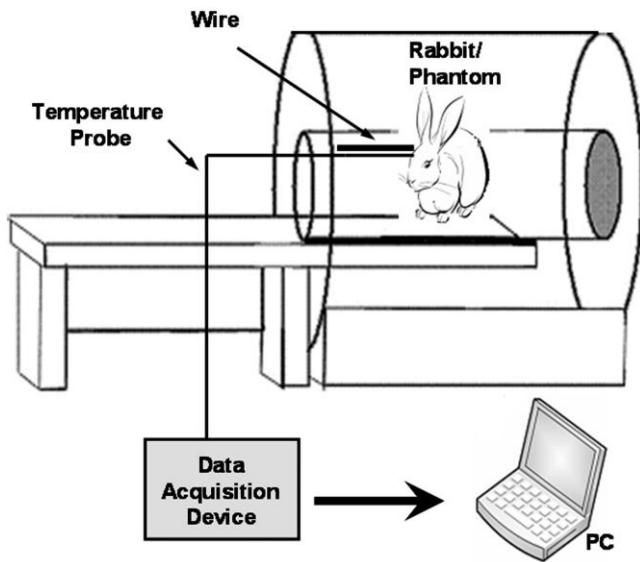


**Figure 4.** Experimental setup of the in vivo and phantom experiments.

RF transmitter, and hence the amount of heat at the wire tip. This geometric variability was kept as controlled as possible by carefully positioning the wire in the same position and orientation in the scanner and at the same depth in the rabbit for each experiment. A fiberoptic probe (FISO Technologies, Ste. Foy, Canada) was attached next to the wire for temperature measurement. The position of the wire and the fiberoptic probe with respect to each other was very crucial in our case, since the sensitive region of the fiberoptic probe was 1 cm behind the tip.

### Phantom Experiment

Ideally, one should make an agarose gel phantom that matches the geometric, electrical, and thermal properties (except perfusion) of the tissue in which the metallic device will be used. In our case, to test the theory, we used a cylindrical homogeneous agarose gel phantom (Agarose A5093, Sigma-Aldrich, Steinheim, Germany) which is a high water content (99%) material thus suitable for simulating tissue. The length of the cylindrical phantom was 10 cm and the diameter was 15 cm. Both the phantom and the rabbits weighed  $\approx 2$  kg. The relative electrical permittivity (70) and conductivity (0.56 S/m) of the gel were deduced from measurements at 64 MHz with a Network Analyzer (HP5763, Agilent Technologies, Santa Clara, CA). The specific heat capacity of the phantom was 3880 J/kgK. The values indicate that the phantom best mimics kidney tissue; however, compensation is possible as mentioned previously for other tissues, especially fat, which exhibits different properties than most other tissues.

The experiment lasted for nearly 2000 seconds and the temperature versus time graph of the phantom was used as a reference for the comparison between exact and the predicted steady state temperature values of different tissues.

### Rabbit In Vivo Experiment

The experimental prediction of in vivo temperature change was validated with rabbit experiments ( $n = 8$ ). Animal preparation was performed as follows. First, the rabbit was anesthetized with a mixture of 35 mg/kg ketamine and 5 mg/kg xylazine through intramuscular infusion. Ketamine was repeated each hour.

Experiments were performed on a GE Signa (Waukesha, WI) 1.5T scanner using an steady-state free precession (SSFP) pulse sequence. The transmit gain was fixed to 15–18 dB, overriding any prescan values. Fiber optic temperature data from four tissues (fat, kidney, liver, and brain) were collected and compared with the data taken from the phantom experiment.

### RESULTS

At the end of the phantom experiment a temperature–time curve was obtained for different input powers. All the curves were normalized with respect to the power applied in the phantom experiment. This normalized temperature–time curve was the reference point of our preceding calculations. Predicted temperature rise corresponding to the four different tissue types (fat, brain, liver, kidney) were calculated from thermal parameters obtained from the literature (Fig. 5).

Two sets of experiments were conducted. In the first set, one phantom and one animal experiment were done. In the second set, one phantom experiment and seven animal experiments were conducted. The data for the second set of experiments are shown in Fig. 6. The regions shown with dashed lines refer to estimated ranges based on phantom experiments for each tissue.

The results of all experiments are summarized in Table 2. The average of temperature increase in in vivo and phantom data of all experiments are calculated for each tissue type separately. The difference between the predicted temperature rise and this averaged value are reported as errors. Given the high variability of in vivo experiments, it is not possible to deduct a definite con-

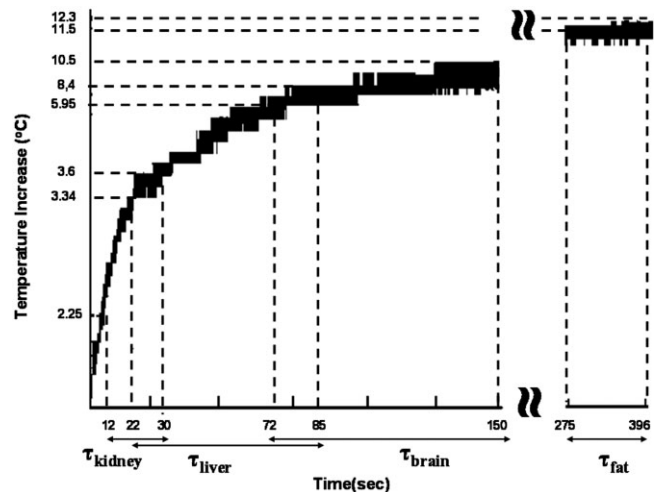


**Figure 5.** The result of the phantom experiment. The perfusion time constants of four tissues (fat, liver, kidney, and brain) and corresponding temperature increases are shown.

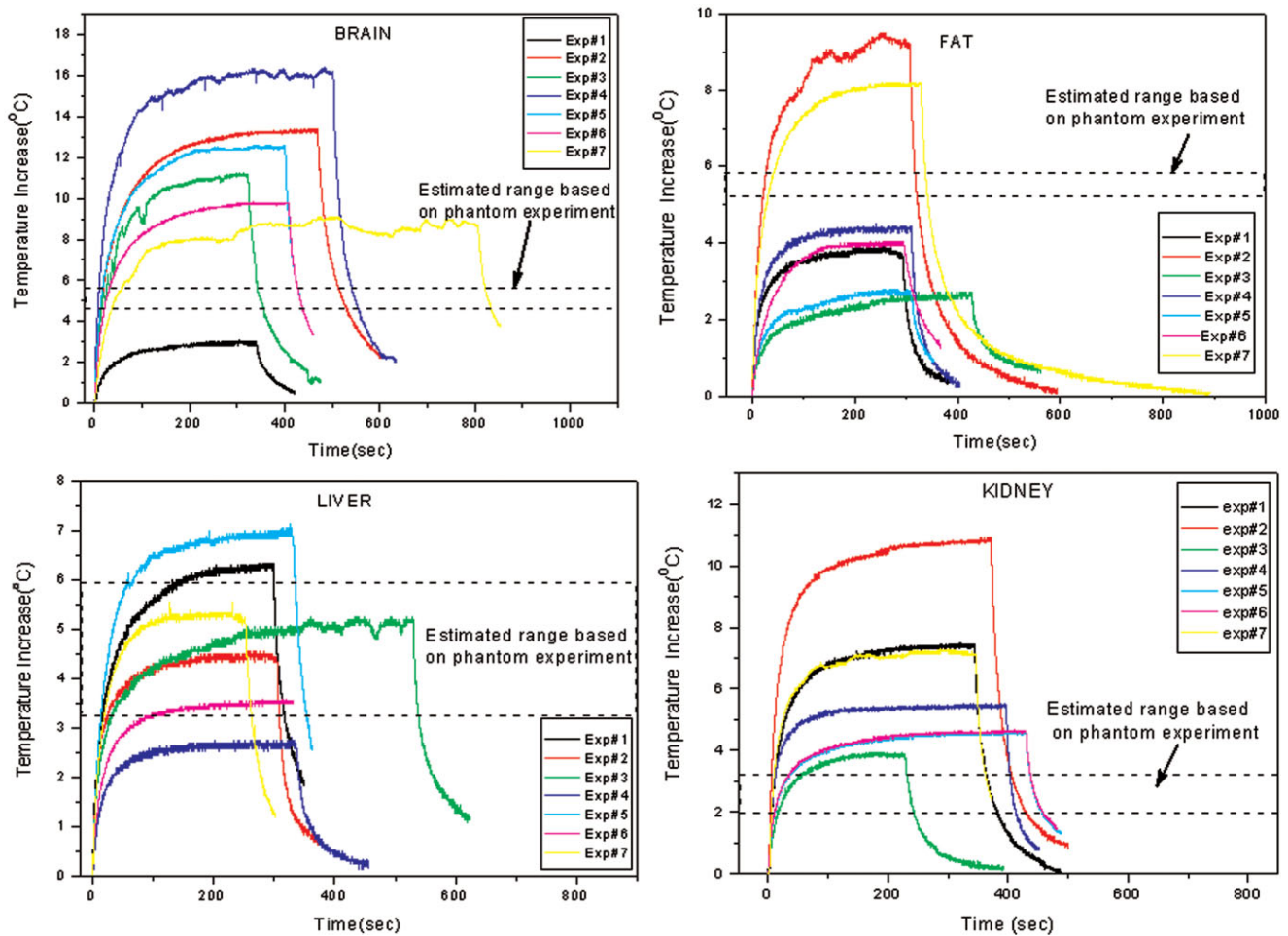


**Figure 6.** Temperature increase versus time graphs for four tissues of rabbit. The regions shown by dashed lines are estimated ranges based on the phantom experiment. Phantom data scaled by heat capacity and applied power of corresponding tissues.

clusion on the errors as a function of the tissue type. Instead, an overall average of 30.8% error can be given as the amount of underestimation with proposed method. This error is within the variability of in vivo experiments (45%).

**DISCUSSION**

In reality, the device under investigation may be placed in several tissues. In such occasions the perfusion time constant of the tissue that contains the hotspot is to be taken into account, since the greatest temperature increase is determined by this local area. Thus, the prediction method described here is not limited to homogeneous tissue.

In the experiment the criterion for choosing the length of the wire was to ensure high signal-to-noise ratio (SNR) temperature data (>2°C temperature increase) to be observed. This could also be achieved using different wire length, inserted length, wire radial position, phantom radial position, and transmit gain parameter. The sequence is also not a determining parameter for the experiment; the prediction is valid once conditions in the phantom experiment mimic the in vivo conditions.

While describing the mathematical background on the proposed temperature rise prediction method, it was shown that even if all the thermal and electrical properties of the gel phantom and the tissue match,

Table 2  
Comparison of Average Values of Predicted and Measured Temperature Increases for Different Tissues

Tissue Type	Average Value of In Vivo Temperature Increase (°C)	Average Value of Scaled Estimated Temperature Increase (°C) (calculated from phantom data at $t = \tau$ )	Average Error in Estimate (%)
Fat	5.7	6.0	5.0
Kidney	6.3	2.7	-57.0
Liver	4.6	3.7	-19.0
Brain	9.2	4.4	-52.0

there may be up to 30% overestimation in the predicted temperature rise based on the distribution of the SAR. Given the variability in the tissue thermal and electrical properties, this error is relatively insignificant. Here we will concentrate on the other error sources.

After doing several phantom and in vivo experiments, an average 30.8% underestimation with our temperature prediction method was observed. As can be seen from Table 2, the temperature increase is overestimated in fat and for liver, kidney, and brain it is underestimated. Two of four experiments have errors within 30%. There may be several reasons for this error.

One reason for the error is the mismatch between thermal and electrical properties of the phantom and the tissues. More accurate results may be obtained if different gels were used for simulating each tissue. Electrical properties of the gel phantom and all the tissues (except fat) are similar (<http://www.fcc.gov/fcc-bin/dielec.sh>), but we did not attempt to match the thermal conductivity of the phantom to the tissues. Both the phantom and tissues involved in these experiments (except fat) are water-dominant; therefore, specific heat capacity values are expected to be similar.

To overcome the temperature fluctuations in animal experiments, it is suggested to use isolated perfused bovine tongue rather than in vivo (24). Although isolated perfused bovine tongue models the perfusion, it is not a perfect model. It lacks body thermal regulation. Electrical and thermal properties of tongue are different than other parts of the body. In addition, this method will introduce extra error sources such as nonuniformity of perfusion. In our studies we used an in vivo animal model that has also its own problems, but obtaining more realistic results is possible using this method.

Another possible source of error is the mismatch between the perfusion values gathered from the literature and the actual in vivo experiment. To minimize the error a wide range of perfusion values from several sources were gathered, as seen in Table 1.

In local heating, thermal diffusivity also plays a significant role. The diffusivity of phantom was measured as  $0.15 \text{ mm}^2/\text{s}$ ; this value is higher than the diffusivity of tissue as seen in Table 1. This results in underestimation of the temperature with phantom experiments.

Last, but not least, placement errors of the temperature probe during experiments introduce significant errors. The temperature rise is local. If the position of the temperature probe varies even less than a millimeter between in vivo and phantom experiments, there will be significant mismatch between results. In order to minimize this error, we paid maximum attention to this problem. However, neither agarose nor body is transparent and, therefore, it was not possible to observe if there was a change in the position of the probe. We believe that this is a significant source of the experimental errors and may explain the high variability of our in vivo experiments. Calculated average bias may have some contribution to this problem.

Although there are some experimental errors and bias, we believe that the proposed in vivo temperature prediction method is a useful method for measuring the

safety of interventional devices or metallic implants inside the body during an MRI examination.

In conclusion, conflicting methods on the evaluation of RF heating in the MR literature led us to construct a practical method for measuring local RF heating. In this study we have presented a method of predicting in vivo temperature increase by using a straightforward agarose gel phantom experiment. We propose that the steady-state tissue temperature is the phantom temperature change for a period of the tissue perfusion time constant. The proposed method was explained by a theory and was tested with several phantom and in vivo experiments. We believe that by reliable test techniques such as the one described here the amount of possible temperature rise in the body with an implant during an MRI exam will be predicted accurately. With the aid of this reliable prediction the amount of power delivered by the scanner will be controlled, enabling safe MRI examinations of patients with implants.

## REFERENCES

1. Nitz WG, Oppelt A, Renz W, Manke C, Lenhart M, Link J. On the heating of linear conductive structures as guidewires and catheters in interventional MRI. *J Magn Reson Imaging* 2001;13:105-114.
2. Yeung CJ, Atalar E. A Green's function approach to local RF heating in interventional MRI. *Med Phys* 2001;28:826-832.
3. Shellock FG. Radiofrequency energy-induced heating during MR procedures: a review. *J Magn Reson Imaging* 2000;12:30-36.
4. Sommer T, Vahlhaus C, Lauck G, et al. MR imaging and cardiac pacemakers: in vitro evaluation and in vivo studies in 51 patients at 0.5 T. *Radiology* 2000;215:869-879.
5. Tronnie VM, Stauber A, Hähnel S, Sarem-Aslani A. Magnetic resonance imaging with implanted neurostimulators: An in vitro and in vivo study. *Neurosurgery* 1999;44:118-125.
6. Ladd ME, Quick HH. Reduction of resonant RF heating in intravascular catheters using coaxial chokes. *Magn Reson Med* 2000;43:615-619.
7. Achenbach S, Moshage W, Diem B, Biebler T, Schibgilla V, Bachmann K. Effects of magnetic resonance imaging on cardiac pacemakers and electrodes. *Am Heart J* 1997;134:467-473.
8. Smith CD, Kildishev AV, Nyenhuis JA, Foster KS, Bourland JD. Interactions of magnetic resonance imaging radio frequency magnetic fields with elongated medical implants. *J Appl Phys* 2000;87:6188-6190.
9. Nyenhuis JA, Kildishev AV, Bourland JD, Foster KS, Graber G, Athey TW. Heating near implanted medical devices by the MRI RF-magnetic field. *IEEE Trans Magn* 1999;35:4133-4135.
10. Shellock FG. Metallic neurosurgical implants: evaluation of magnetic field interactions, heating, and artifacts at 1.5-Tesla. *J Magn Reson Imaging* 2001;14:295-299.
11. Yeung CJ, Atalar E. Estimating in vivo temperature changes due to localized RF heating from interventional devices. In: *Proc 9th ISMRM, Glasgow, Scotland*; 2001:1756.
12. Smith CD, Nyenhuis JA, Foster KS. A comparison of phantom materials used in evaluation of radiofrequency heating of implanted medical devices during MRI. In: *Proc 23rd Annual International Conference IEEE Eng Med Biol Soc, Istanbul*; 2001.
13. Busch HJM, Vollmann W, Schnorr J, Grönemeyer HWD. Finite volume analysis of temperature effects induced by active MRI implants with cylindrical symmetry. *BioMed Eng OnLine* 2005;4:25-42.
14. Yeung CJ, Atalar E. RF transmit power limit for the barewire loopless catheter antenna. *J Magn Reson Imaging* 2000;12:86-91.
15. Luechinger R, Weber OM, Bieler M, Boesiger P. Heat distribution near pacemaker lead tips. In: *Proc 9th Annual Meeting ISMRM, Glasgow, Scotland*; 2001:1759.
16. Pennes HH. Analysis of tissue and arterial temperatures in the resting human forearm. *J Appl Physiol* 1948;1:93-122.
17. Nevels RD, Arndt GD, Raffoul GW, Carl JR, Pacifico A. Microwave catheter design. *IEEE Trans Biomed Eng* 1998;45:885-890.

18. Cooper TE, Trezek GJ. Correlation of thermal properties of some human tissue with water content. *Aerospace Med* 1971;42:24–27.
19. Valvano JW, Cochran JR, Diller KR. Thermal conductivity and diffusivity of biomaterials measured with self-heated thermistors. *Int J Thermophys* 1985;6:301–311.
20. Guy AW, Lehmann JF, Stonebridge JB. Therapeutic applications of electromagnetic power. In: *Proc IEEE* 1974;62:55–75.
21. Tropea BI, Lee RC. Thermal injury kinetics in electrical trauma. *J Biomech Eng* 1992;114:241–250.
22. Shitzer A, Eberhart RC. Heat transfer in medicine and biology. New York: Plenum; 1985. p 141.
23. Yeung CJ, Susil RC, Atalar E. RF safety of wires in interventional MRI: Using a safety index. *Magn Reson Med* 2002;47:187–193.
24. Raaymakers BW, Crezee J, Lagendijk JJW. Modelling individual temperature profiles from an isolated perfused bovine tongue. *Phys Med Biol* 2000;45:765–780.
25. Ocali O, Atalar E. Intravascular magnetic resonance imaging using a loopless catheter antenna. *Magn Reson Med* 1997;37:112–118.
26. Polk C, Postow E. Handbook of biological effects of electromagnetic fields, 2nd ed. New York: CRC Press; 1996. p 92–93.
27. U.S. Department of Health and Human Services, Food and Drug Administration, Center for Devices and Radiological Health. Guidance for the submission of premarket notifications for magnetic resonance diagnostic devices. Rockville, MD: US DHHS FDA; 1998.
28. International Electrotechnical Commission. Medical electrical equipment. Part 2. Particular requirements for the safety of magnetic resonance equipment for medical diagnosis. International Standard 60601-2-33. Geneva: IEC; 1995.
29. Hirate A, Watanabe S, Kojima M, et al. Computational verification of anesthesia effect on temperature variations in rabbit eyes exposed to 2.45 GHz microwave energy. *Bioelectromagnetics* 2006; 27:602–612.
30. Materne R, Beers BE, Smith AM, et al. Non-invasive quantification of liver perfusion with dynamic computed tomography and a dual-input one-compartmental model. *Clin Sci* 2000;99:517–525.
31. Jones SC, Parker DS. Mammary blood flow and cardiac output in the conscious lactating rabbit. *J Comp Physiol* 1980;138:31–34.
32. Anetzberger H, Thein E, Becker M, Walli AK, Messmer. Validity of fluorescent microspheres method for bone blood flow measurement during intentional arterial hypotension. *J Appl Physiol* 2003;95: 1153–1158.
33. Eyret JA, Essex TJH, Flecknell PA, Bartholomew PH, Sinclair JI. A comparison of measurements of cerebral blood flow in the rabbit using laser Doppler spectroscopy and radionuclide labelled microspheres. *Clin Phys Physiol Meas* 1988;9:65–74.
34. Carroll JF, Huang M, Hester RL, Cockrell K, Mizelle L. Hemodynamic alterations in hypertensive obese rabbits. *Hypertension* 1995;26:465–470.